

HumanEgo: Zero-Shot Robot Learning from Minutes of Human Egocentric Videos

Zhi (Leo) Wang Botao He Kelin Yu Seungjae Lee
 Ruohan Gao Furong Huang Yiannis Aloimonos
 University of Maryland
<https://humanego-ai.github.io/>

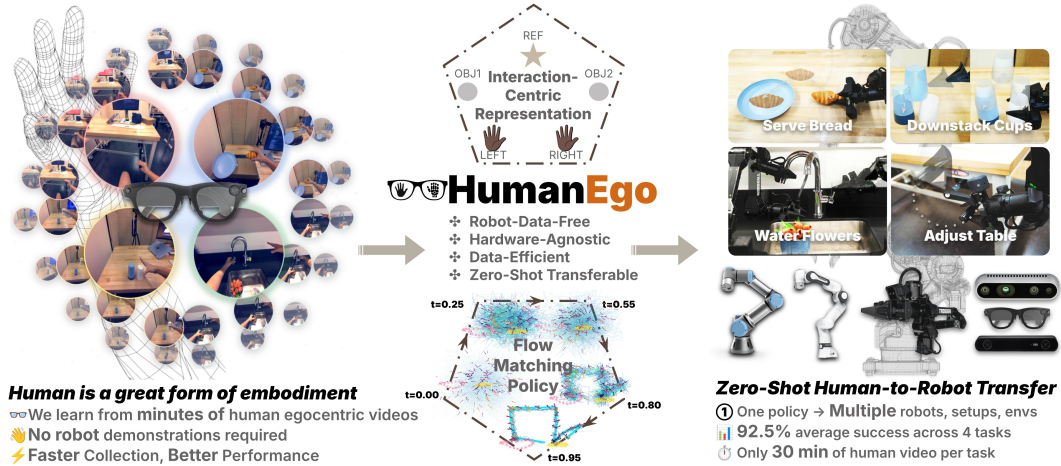


Fig. 1: **HumanEgo learns robot policy from human egocentric videos.** A human wears Aria glasses and collects demonstrations (left); the egocentric videos are converted into an interaction-centric representation and used to train a flow matching policy (middle); the policy transfers *zero-shot* to the robot—free of environment, setup, or embodiment (right).

Abstract: Human egocentric video captures rich manipulation demonstrations without any robot hardware, yet transferring these skills to robots remains challenging due to the embodiment gap between human and robot in both visual appearance and kinematics. We present **HumanEgo**, a framework that bridges the embodiment gap by lifting each human demonstration to an entity-level representation of *hand-object interaction*, and training a *flow matching* policy with *dense auxiliary objectives* that amplify supervision from every trajectory. HumanEgo is robot-data-free, hardware-agnostic, data-efficient, and zero-shot human-to-robot transferable. With only 30 minutes of human videos per task, HumanEgo achieves **92.5%** average success across four real-world tasks (**75%** with just 15 minutes), outperforms matched-time robot teleoperation by **41%**, and robustly transfers zero-shot across novel robots, cameras, and environments.

Keywords: Human-to-Robot Transfer, Egocentric Videos, Efficient Learning

1 Introduction

State-of-the-art manipulation policies require hundreds to thousands of task-specific robot demonstrations [1, 2, 3, 4], which are costly, time-consuming, and inconvenient to collect. Human egocentric video offers a much cheaper and more accessible alternative: with a head-mounted camera [5], a single person can collect task demonstrations anywhere, in minutes. But how should we leverage this data? Existing approaches fall into two paradigms, each with significant limitations. *Co-training* methods [6, 7] supplement robot data with human video, but still require substantial robot demonstrations for every new task—reducing, rather than eliminating, the data burden. *Large-scale pretraining* approaches [8, 9] learn from massive egocentric corpora, but demand enormous compute and still require robot-specific post-training to produce deployable policies. We pursue a more

direct goal: **learning deployable manipulation policies from only minutes of human egocentric demonstrations—without any robot data and internet-scale pretraining.**

Achieving this goal exposes two fundamental challenges. **(1) The representation challenge: bridging the embodiment gap.** Humans and robots differ in both *visual appearance* and *kinematics*, and these gaps demand distinct solutions. On the visual side, retargeting-based methods [10, 11] synthesize robot-like imagery from human video but are brittle to morphological and viewpoint differences; point-tracking approaches [12, 13] extract sparse geometric features but discard the rich visual context surrounding interactions. On the kinematic side, hierarchical methods [14, 15] separate high-level plans from low-level execution but still require robot data for the low-level controller; object-centric approaches [16, 17] track only the manipulated object, losing critical information about *how* the hand approaches, grasps, and releases it. We argue that neither hand nor object alone defines a skill—what matters is their *interaction*.

(2) The learning challenge: learning from minimal data. Although raw human video is abundant online, clean clips with precise action labels remain scarce, making data-efficient learning from minutes of per-task videos critical. This regime introduces two distinct challenges: *multi-modality* and *signal sparsity*. For the multi-modality challenge, the same task admits many valid strategies. Diffusion-based methods [4] capture this distribution but need many denoising steps and are slow at inference; faster alternatives [18] are less expressive. For the signal-sparsity challenge, each trajectory carries rich signal beyond the hand action—object motion, visual traces, hand–object state—yet prior work taps only a fraction: single auxiliary targets such as visual foresight [16] or 2D tracks [12], or upstream pretraining corpora [8, 9]. We argue that a fast generative policy paired with multi-type dense supervision is the key to data-efficient learning from minutes of human egocentric videos.

We present HumanEgo, addressing each gap with a targeted design. For the *visual gap*, we in-paint the human arm from each egocentric frame and render a virtual gripper with tracked object keypoints in its place, producing an embodiment-agnostic visual observation. For the *kinematic gap*, we encode every hand and object as an Interaction-Centric Token (ICT), producing a compact, embodiment- and viewpoint-invariant spatial observation of hand–object interaction. For *multi-modality*, we adopt a flow matching [19] policy, producing expressive multi-modal actions at fast inference. For *signal sparsity*, we design three dense auxiliary objectives: 2D trace, object motion, and latent consistency. Together they produce multi-type dense supervision from each trajectory’s scene dynamics, boosting learning from few demonstrations. Our contributions:

- **HumanEgo**, a robot-data-free, hardware-agnostic, and data-efficient pipeline that learns robot manipulation policies from minutes of raw human egocentric videos—powered by a flow matching policy with dense auxiliary objectives.
- **Interaction-Centric Tokens (ICT)**, a compact entity-level representation of hand–object interaction invariant to embodiment, viewpoint, and environment.
- **Robust zero-shot human-to-robot transfer.** Trained on 30 minutes of human video per task, HumanEgo reaches **92.5%** success across 4 real-world tasks and **75%** at half that budget. At matched collection time, it surpasses robot teleoperation by **41%**. The learned policy also deploys zero-shot to novel robot embodiments, camera setups, lighting, backgrounds, and object instances, without any retraining or fine-tuning. This suggests that, with the right framework, human video is not merely a cheap substitute but a *superior* data source for policy learning.

2 Related Work

Learning manipulation from human video is appealing yet difficult: the *embodiment gap* between human hands and robot grippers obstructs direct transfer. Early work learned task plans from third-person video [20, 21], but viewpoint mismatch limited real-world transfer, and egocentric video has since become the dominant paradigm. Subsequent methods attack the embodiment gap along two complementary axes: augmenting human data with robot data or large-scale pretraining, or designing observations that abstract over the agent’s body. **(i) Bridging via robot data or pretrain-**

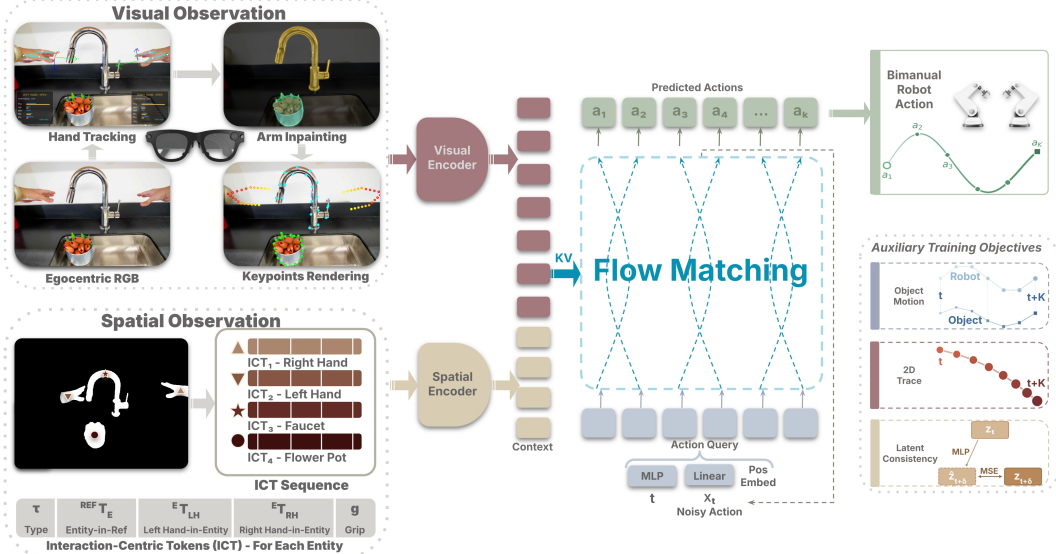


Fig. 2: **System overview of HumanEgo.** Arm inpainting and visual keypoints bridge the visual gap; Interaction-Centric Tokens encode spatial relationships among all entities; a flow matching policy with dense auxiliary objectives learns bimanual robot actions from minutes-scale human data.

ing. *Visual retargeting* [10, 15, 22] renders robot morphology into human scenes to manufacture pseudo-demonstrations, but the rendered imagery is brittle to morphological and viewpoint variations; *hierarchical* approaches [14] learn high-level plans from human data but still rely on robot demonstrations for the low-level controller; *co-training* strategies [6, 7, 17] jointly optimize over human and robot data, reducing rather than eliminating the robot-data requirement; and *large-scale pretraining* [8, 9] bets on massive egocentric corpora at the cost of enormous compute and robot-specific post-training. **(ii) Bridging via representation: zero-shot transfer.** A second line eliminates robot data entirely by reformulating observations into embodiment-agnostic representations—the space HumanEgo occupies. We compare against each of the following five methods in Sec. 4.1. **EgoZero** [11] lifts the scene into egocentric 3D point clouds, achieving morphology-agnostic transfer but treating hands and objects as undifferentiated points. **Point Policy** [13] learns from sparse tracked keypoints on both hand and object, gaining computational efficiency over dense point clouds but losing global scene context. **ZeroMimic** [23] distills 3D wrist trajectories from web videos via structure-from-motion, enabling zero-shot transfer but requiring goal specification at test time. **Track2Act** [12] predicts 2D point tracks from internet videos to derive manipulation plans, foregoing 3D reasoning entirely. **SPOT** [24] generates SE(3) object pose trajectories via diffusion, capturing object dynamics but modeling the manipulator only implicitly. A common thread: these methods represent the hand *or* the object, but rarely their *interaction*—the signal that defines manipulation. HumanEgo bridges this gap with an *interaction-centric* representation encoding the spatial relationship between hands and objects.

3 HumanEgo

HumanEgo turns human egocentric video into a deployable bimanual policy in four stages (Fig. 2). A demonstrator wearing Aria glasses records the task (Sec. 3.1); we close the *embodiment gap* by inpainting the human arm and rendering a virtual gripper (Sec. 3.2) and by encoding every entity’s pose relative to other task entities into Interaction-Centric Tokens (Sec. 3.3). A flow matching policy with three auxiliary objectives generates multi-modal bimanual actions (Sec. 3.4).

3.1 Egocentric Data Collection

A human demonstrator wearing Aria Gen1 glasses [5] performs the target task in any convenient environment—regardless of table height, lighting, or background, and without specialized workspace or calibration (Fig. 11; App. A). Each demonstration takes only seconds; we collect around 30 minutes of human demonstrations per task at 30 Hz. Aria glasses are particularly well

suited for learning from human video: their Machine Perception Services (MPS) provide high-quality 6-DoF SLAM tracking, calibrated 3D hand pose estimation, and synchronized egocentric RGB streams—all from a single lightweight wearable device.

3.2 Visual Observation Preprocessing

We transform the undistorted egocentric frames into embodiment-agnostic RGB observations in two steps. First, we segment the human hand and arm with SAM2 and remove them via LaMa inpainting [25], eliminating the visual embodiment gap. Second, we render a virtual gripper and the tracked object keypoints into the inpainted image—both derived from the spatial observation (Sec. 3.3)—implicitly encoding 6D pose information as visual cues. This lightweight procedure bridges the visual embodiment gap without expensive domain adaptation or image translation.

3.3 Spatial Observation Preprocessing

We build our explicit entity-level spatial observation: treating every object and both hands as an *entity*, we track the hands and objects to recover each entity’s 6-DoF pose, then encode their relative relations into Interaction-Centric Tokens. We detail these three steps below:

Hand tracking and motion optimization. We start from the 3D hand keypoints produced by Aria MPS [5], lift them to the world frame via SLAM, and smooth them with Savitzky–Golay on positions and an exponential moving average (EMA) on rotations. We then treat the thumb–index pair as a virtual parallel-jaw gripper (Fig. 12), extracting an SE(3) end-effector pose T_{ee} and a scalar grasp g . For *position*, we take the fingertip midpoint $\mathbf{p}_{ee} = (\mathbf{p}_{\text{thumb}} + \mathbf{p}_{\text{index}})/2$. For *orientation*, we build a Gram–Schmidt frame on the metacarpophalangeal (MCP) joints rather than the fingertips, $R_{ee} = \text{GramSchmidt}(\mathbf{x}: \text{thumb MCP} \rightarrow \text{index MCP}, \mathbf{y}: \text{wrist} \rightarrow \text{MCP mid})$, where MCP mid is the midpoint of the two MCPs; this avoids the degeneracy when fingertips converge during pinch grasps. For *grasp*, we compute a scalar $g \in [0, 1]$ by normalizing the thumb–index fingertip distance (details in App. B.3), and binarize at deployment.

Object tracking and pose estimation. We detect each object with text-prompted Grounding DINO [26], segment it with SAM2 [27], and sample contour keypoints from the mask. We track these 2D keypoints \mathbf{u}_n across the video with CoTracker3 [28] and lift them to 3D via $\mathbf{p}_n = \text{Triangulate}(\mathbf{u}_n, K, T_{\text{SLAM}})$, using camera intrinsics K and the per-frame Aria SLAM pose T_{SLAM} . We take the centroid of the N tracked points as the object position to cancel per-point triangulation noise, $\mathbf{p}_{\text{obj}} = \frac{1}{N} \sum_{n=1}^N \mathbf{p}_n$, and estimate orientation R_{obj} with Orient-Anything V2 [29]. During grasping the object is occluded by the hand, so we apply *kinematic latching*—rigidly tying the object pose to the hand from the grasp onset t_0 : $T_{\text{obj}}^t = T_{\text{hand}}^t \cdot (T_{\text{hand}}^{t_0})^{-1} T_{\text{obj}}^{t_0}$.

Entity Spatial Encoding via Interaction-Centric Tokens (ICT). We encode each entity’s 6-DoF pose into an ICT, capturing both its pose in a shared reference frame and its spatial relation to both hands. For each entity $k=1, \dots, N$, the token $\text{ICT}_k \in \mathbb{R}^{29}$ is:

$$\text{ICT}_k = \left[\underbrace{\tau}_1 \parallel \underbrace{{}^{\text{REF}}T_E}_9 \parallel \underbrace{{}^E T_{LH}}_9 \parallel \underbrace{{}^E T_{RH}}_9 \parallel \underbrace{g}_1 \right], \quad (1)$$

where τ is the entity type (hand or object); ${}^{\text{REF}}T_E$ is entity k ’s pose in a shared reference frame REF (a static camera frame); ${}^E T_{LH}$ and ${}^E T_{RH}$ are the left-hand (LH) and right-hand (RH) poses expressed in entity k ’s local frame E ; and g is the grasp state (binarized finger distance for hands; a sentinel for objects). We flatten each SE(3) transform to a 9D vector by concatenating the normalized translation with a 6D rotation representation [30], and derive every quantity from off-the-shelf perception without ground-truth labels. Unlike prior methods using global point clouds or absolute coordinates [11, 13], we anchor each ICT to an entity so that the evolving ${}^E T_{LH}$ and ${}^E T_{RH}$ directly reflect the manipulation state—approaching, grasping, or transporting—making the representation inherently *interaction-centric*. Expressing every quantity relative to scene entities rather than the camera yields identical tokens regardless of viewpoint, enabling direct human-to-robot transfer. We also gain a unified, variable-length interface that accommodates scenes with different numbers of objects without architectural changes. We empirically show that ICT is the key enabler of cross-embodiment transfer (Sec. 4.4).

3.4 Flow Matching Policy with Dense Auxiliary Objectives

Our policy (Fig. 2) takes the scene state s_t —ICT tokens and an RGB image—and generates a bi-manual action trajectory $\mathbf{a} \in \mathbb{R}^{K \times D_a}$ over a K -step horizon, where each D_a -dim slice concatenates both hands’ 6-DoF poses and binary grasps. We describe the training below.

Flow matching action generation. We formulate action generation as a conditional flow matching [19, 31] problem: we parameterize a velocity field v_θ with a transformer decoder conditioned on s_t , and train it to transport a Gaussian prior sample to the action target. Our primary training loss is:

$$\mathcal{L}_{\text{FM}} = \mathbb{E}_{t, \mathbf{x}_0, \mathbf{x}_1} \left[w_p \|\Delta \mathbf{p}\|^2 + w_r \|\Delta \mathbf{r}\|^2 + w_g \|\Delta g\|^2 \right], \quad \mathbf{x}_t = (1-t) \mathbf{x}_0 + t \mathbf{x}_1, \quad (2)$$

where w_p, w_r, w_g are the loss weights for position (\mathbf{p}), rotation (\mathbf{r}), and grasp (g); $\Delta(\cdot) = v_\theta(\mathbf{x}_t, t, s_t) - (\mathbf{x}_1 - \mathbf{x}_0)$ is the velocity prediction error; $\mathbf{x}_t = (1-t)\mathbf{x}_0 + t\mathbf{x}_1$ is the interpolated sample at flow time $t \sim \mathcal{U}(0, 1)$; $\mathbf{x}_0 \sim \mathcal{N}(\mathbf{0}, \mathbf{I})$ is a Gaussian prior sample; and \mathbf{x}_1 is the ground-truth bimanual action. At inference, we integrate the learned ODE with a fixed-step Euler solver.

Dense auxiliary objectives. To extract rich supervision from every demonstration, we add three auxiliary objectives that share the context encoder with the flow matching head: (1) *Object motion* (\mathcal{L}_{OM}): we predict each manipulated object’s future 6-DoF trajectory, forcing the encoder to model object dynamics under hand motion; (2) *2D trace* (\mathcal{L}_{2D}): we regress future 2D projections of entity trajectories, grounding the representation in the visual observation; (3) *Latent consistency* (\mathcal{L}_{LC}): we predict the ICT state K steps ahead, pushing the encoder to capture scene dynamics. We combine them with the flow matching loss into a single objective:

$$\mathcal{L} = \mathcal{L}_{\text{FM}} + \lambda_{\text{OM}} \mathcal{L}_{\text{OM}} + \lambda_{\text{2D}} \mathcal{L}_{\text{2D}} + \lambda_{\text{LC}} \mathcal{L}_{\text{LC}}, \quad (3)$$

where $\lambda_{\text{OM}}, \lambda_{\text{2D}}, \lambda_{\text{LC}}$ are the loss weights of the three auxiliary objectives. We derive every auxiliary target automatically from the perception pipeline, so each demonstration yields a dense multi-task signal. All three objectives forecast how the scene evolves in complementary spaces (3D physical, 2D visual, latent space), equipping the shared encoder with a lightweight world model of hand-object interaction. We also exploit the shared encoder as a multi-task regularizer that curbs overfitting, with the largest gains in the low-data regime (Sec. 4.2, 4.4).

4 Experiments

We evaluate HumanEgo to answer four questions: (1) Can the embodiment gap be bridged to achieve reliable manipulation from human video alone? (Sec. 4.1) (2) How does policy performance scale with human data versus matched robot data? (Sec. 4.2) (3) How robust is the policy to distribution shifts in embodiment, viewpoint, and environment? (Sec. 4.3) (4) How much does each component contribute to the final performance? (Sec. 4.4) Unless otherwise noted, all experiments are conducted on Trossen WidowX arms with a top-mounted RealSense D405 (App. D.1), and we report success rate (%) over 40 trials per task with randomized initial object positions.

4.1 HumanEgo Bridges the Embodiment Gap Efficiently

We evaluate HumanEgo on four real-world manipulation tasks (Fig. 3; details in App. A.2): *Serve Bread*, a **pick-and-place** task in which the robot grasps a croissant from arbitrary positions and places it on a plate; *Downstack Cups*, a **long-horizon multi-step** task requiring sequential toppling, grasping, and re-stacking of three nested cups; *Water Flowers*, a **contact-rich bimanual** task with strict temporal ordering—one arm holds a pulled-out spray nozzle over a flower pot while the other opens the valve; and *Adjust Table*, a **sustained rotational-control** task in which the robot grasps a crank handle and turns it three full revolutions without releasing. We compare against five recent zero-shot methods that learn manipulation from human egocentric video—EgoZero [11], Point Policy [13], ZeroMimic [23], Track2Act [12], and SPOT [24] (each described in Sec. 2)—all trained on

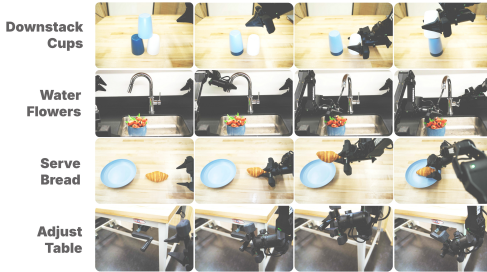


Fig. 3: **Four Real-World Evaluation tasks.**

Overall Real-World Evaluation

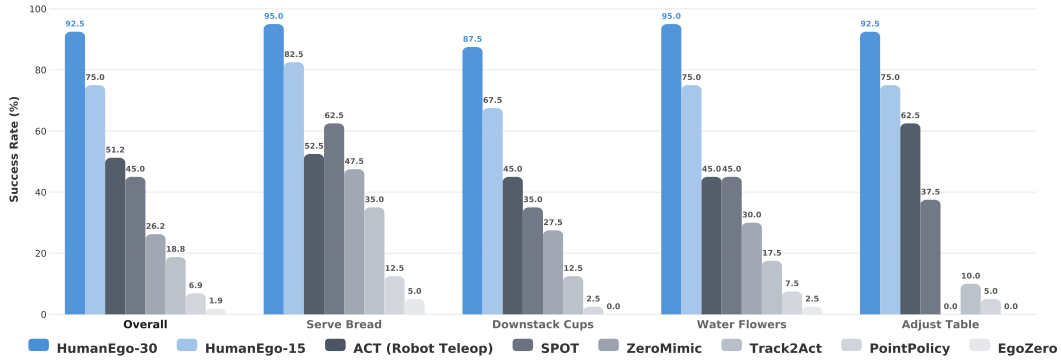


Fig. 4: **Overall Real-World Evaluation.** Real-world success rate (%) for each method across all four tasks. HumanEgo with 30 min of data achieves the highest success rate on every task, demonstrating consistent improvements over both human-video baselines and robot teleoperation methods.

the same 30 minutes of data per task, as well as ACT trained on 30 minutes of robot teleoperation data collected on the same hardware.

HumanEgo achieves the highest success rate on every single task. As shown in Fig. 4, HumanEgo with only 30 minutes of human data reaches **92.5%** average success rate across all four tasks. In contrast, the five human-video baselines range from 1.9% to 45.0%, a wide spread revealing that each method captures only a partial aspect of manipulation, performing adequately on simpler tasks but collapsing on those that demand precise hand-object reasoning. HumanEgo is the only method that maintains high performance regardless of task complexity.

Even with half the data, HumanEgo outperforms robot teleoperation. HumanEgo with only 15 minutes of human data already reaches 75.0%, surpassing ACT trained on 30 minutes of robot teleoperation (51.2%), highlighting the data efficiency of our approach—and that *readily available human videos can be a surprisingly potent data source for robot learning.*

HumanEgo excels on tasks that demand precise coordination and spatial reasoning. On Downstack Cups, a long-horizon task requiring sequential unstacking of three nested cups with ~ 1 cm tolerance where early errors compound, HumanEgo reaches 87.5% while no baseline exceeds 45%. On Water Flowers, the robot must coordinate both arms sequentially—one arm completes its subtask before the other opens the faucet to pour water—and precisely aim the stream into the pot, demanding genuine spatial understanding of object positions rather than memorized trajectories; HumanEgo achieves 95%, more than double the best baseline (45%).

4.2 The Efficiency of Human Demonstrations

We compare HumanEgo trained on human video against ACT and HumanEgo trained on robot teleoperation as a function of collection time on Serve Bread (Fig. 5).

HumanEgo learns effectively from minimal human data. With only ~ 7 minutes of human demonstrations, HumanEgo already reaches 50% success rate and continues to climb smoothly, reaching 95% at 30 minutes. This steep, monotonic scaling curve indicates that our pipeline extracts useful manipulation signal from even a handful of demonstrations.

Auxiliary objectives amplify learning when demonstrations are scarce. Between 2 and 12 minutes, HumanEgo with auxiliary losses consistently outperforms the variant without them, with the

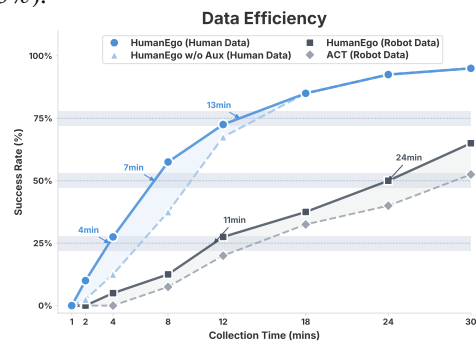


Fig. 5: **Data efficiency.** Success rate (%) vs. data collection time. HumanEgo trained on 8 min of human data surpasses ACT’s 30-min robot data.

largest gain at 8 min (57.5% vs. 37.5%). Beyond 18 minutes both variants converge, reaching 95% at 30 minutes, confirming that auxiliary losses extract richer supervision from each demonstration—a benefit that diminishes as data grows abundant.

Human video is a more efficient data source than robot teleoperation. At 8 minutes of collection time, HumanEgo trained on human video (57.5%) already surpasses ACT trained on 30 minutes of robot teleoperation (52.5%)—a 3.75× reduction in collection effort. Offline metrics further confirm that human demonstrations exhibit greater spatial density and trajectory diversity, producing higher-quality training signal per minute of collection (Fig. 6).

4.3 One Policy, Many Conditions

We deploy HumanEgo on Serve Bread and Downstack Cups across 9 out-of-distribution conditions—without any retraining or fine-tuning (40 trials each for each task; results in Fig. 7, real-world setup in Fig. 8).

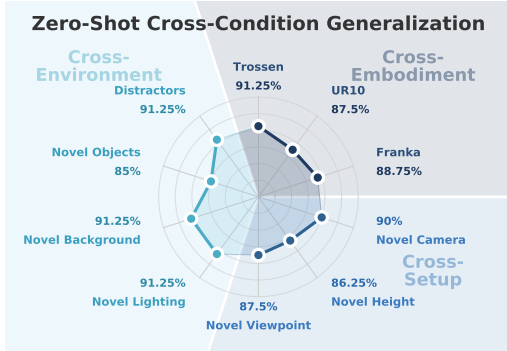


Fig. 7: **Zero-Shot Cross-Condition Generalization.** HumanEgo maintains robust success across different conditions without retraining.

HumanEgo is robust to arbitrary visual conditions. Changing the background, lighting, viewpoint, or adding distractors all yield 85–91.25% success, with no measurable degradation in most cases. The policy even handles novel object instances that never appear in the training set, demonstrating that it effectively extracts task-relevant information from the visual input while remaining invariant to irrelevant variations.

HumanEgo is robust to arbitrary object placements. On Serve Bread, it delivers the bread to the plate across arbitrary absolute and relative positions on the table and even at novel heights; on Downstack Cups, it completes the three-step sequence under varied table heights and cup positions—scenarios where methods like EgoZero [11] and PointPolicy [13] often fail. Beyond this quantitative evaluation, we also observe similar placement robustness qualitatively on Water Flowers, where the robot aims the faucet into the pot wherever it sits in the sink. This robustness reflects the object-centric structure embedded in our interaction-centric representation, enabling placement invariance.

HumanEgo is hardware-agnostic. All training data is collected with Aria glasses, yet at inference the policy achieves high success rates regardless of the deployment hardware—whether the camera is a RealSense or a ZED, and whether the robot arm is a Trossen, Franka, or UR10. The training and deployment setups share no hardware in common, yet the policy transfers seamlessly—enabled by the frame-invariant representation and training architecture detailed in Sec. 4.4.

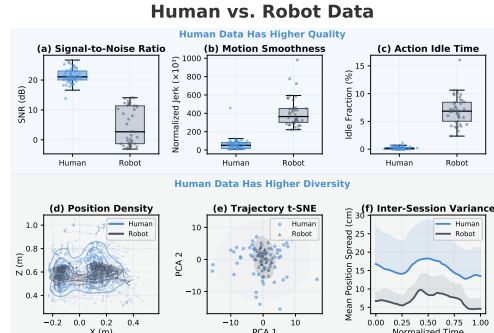


Fig. 6: **Human vs. robot data.** Human egocentric data exhibits higher SNR, smoother motion, less idle time (top), and greater spatial and trajectory diversity (bottom).



Fig. 8: **Cross-condition real-world evaluation:** cross-embodiment / environment / setup.

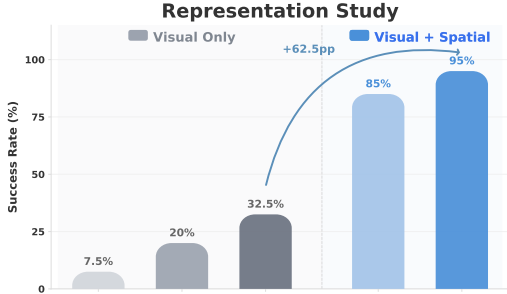


Fig. 9: **Representation study.** Success rate (%) for five input configurations. Visual-only methods plateau at 32.5% with any strategy; adding spatial tokens yields +52.5 pp.

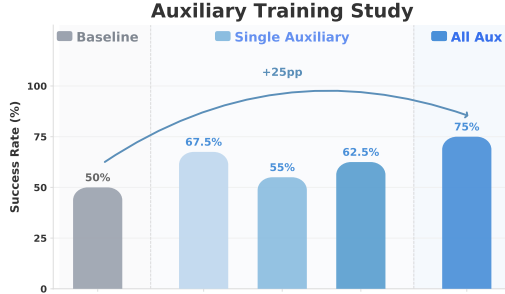


Fig. 10: **Auxiliary training study.** Success rate (%) at 15 min of data for each auxiliary objective individually. Object motion contributes the most (+17.5 pp); all three combine for +25 pp.

4.4 What Drives Performance of HumanEgo?

We ablate HumanEgo’s two core design choices on Water Flowers: the spatial representation (Fig. 9) and the auxiliary training objectives (Fig. 10).

Explicit spatial representation, not visual fidelity, is the key to bridging the embodiment gap.

We isolate visual preprocessing from spatial representation. Progressively reducing the visual embodiment gap—from raw human RGB (7.5%) to keypoint rendering with arm inpainting (20%) to robot RGB that eliminates the gap entirely (32.5%)—yields only modest gains; even with zero visual mismatch, the policy barely exceeds 30%. Monocular RGB encodes *appearance*, not the 3D spatial relationships that manipulation demands. Adding ICT to raw human RGB produces a dramatic jump from 7.5% to 85%, and the full system reaches 95%. ICT directly encodes the relative 6-DoF transforms between hands and objects—the core manipulation state—turning the problem of inferring 3D dynamics from pixels into learning actions from explicit spatial relationships.

Auxiliary objectives provide complementary gains. We evaluate each objective individually at 15 minutes of data. Each loss independently improves performance: object motion (+17.5 pp), latent consistency (+12.5 pp), and 2D trace (+5 pp). Combined, they yield a cumulative +25 pp improvement over the base model. At a high level, all three objectives perform forward dynamics prediction—forecasting how manipulation states evolve—in different spaces (3D physical space, 2D visual space, and latent state embeddings), forcing the shared encoder to learn the causal structure of manipulation rather than visual appearance alone.

5 Conclusion

We presented **HumanEgo**, a framework that learns robot manipulation policies from minutes of human egocentric videos—without any robot data or large-scale pretraining. HumanEgo adopts a hardware-agnostic representation that bridges the embodiment gap through visual preprocessing (arm inpainting, keypoint rendering) and spatial encoding (ICT), making the learned policy invariant to embodiment, viewpoint, and environment. Combined with a flow matching policy and dense auxiliary objectives that supervise forward dynamics in complementary spaces, HumanEgo achieves 92.5% average success across four real-world tasks, outperforms five recent human-video baselines, yields a 41% improvement over matched-time robot teleoperation, and generalizes zero-shot to novel robot embodiments, camera setups, and real-world environments—without any retraining.

Limitations and future work. Our framework relies on Aria’s stereo hand tracking—monocular substitutes degrade performance (App. E.1), calling for stronger monocular hand pose estimators. We use per-frame object detection rather than real-time tracking; in-hand manipulation and other dynamic scenarios will require real-time trackers. The pipeline chains several off-the-shelf perception modules whose failures cascade, motivating stronger or jointly-trained frontends. Finally, few-shot learning plateaus at ~ 1 cm precision, beyond which reinforcement learning or related approaches become necessary.

Acknowledgments

We thank the anonymous reviewers for their constructive feedback.

References

- [1] A. Brohan, N. Brown, J. Carbajal, Y. Chebotar, X. Chen, K. Choromanski, T. Ding, D. Driess, A. Dubey, C. Finn, P. Florence, C. Fu, M. G. Arenas, K. Gopalakrishnan, K. Han, K. Hausman, A. Herzog, J. Hsu, B. Ichter, A. Irpan, N. Joshi, R. Julian, D. Kalashnikov, Y. Kuang, I. Leal, L. Lee, T.-W. E. Lee, S. Levine, Y. Lu, H. Michalewski, I. Mordatch, K. Pertsch, K. Rao, K. Reymann, M. Ryoo, G. Salazar, P. Sanketi, P. Sermanet, J. Singh, A. Singh, R. Soricut, H. Tran, V. Vanhoucke, Q. Vuong, A. Wahid, S. Welker, P. Wohlhart, J. Wu, F. Xia, T. Xiao, P. Xu, S. Xu, T. Yu, and B. Zitkovich. RT-2: Vision-language-action models transfer web knowledge to robotic control. *arXiv preprint arXiv:2307.15818*, 2023.
- [2] Octo Model Team, D. Ghosh, H. Walke, K. Pertsch, K. Black, O. Mees, S. Dasari, J. Hejna, T. Kreiman, C. Xu, J. You, J. Wu, and S. Levine. Octo: An open-source generalist robot policy. *arXiv preprint arXiv:2405.12213*, 2024.
- [3] ALOHA 2 Team, J. Aldaco, T. Armstrong, R. Baruch, J. Bingham, S. Chan, K. Draper, D. Dwibedi, C. Finn, P. Florence, S. Goodrich, W. Gramlich, T. Hage, A. Herzog, J. Hoech, T. Nguyen, I. Storz, B. Tabanpour, L. Takayama, J. Tompson, A. Wahid, T. Wahrburg, S. Xu, S. Yaroshenko, K. Zakka, and T. Z. Zhao. ALOHA 2: An enhanced low-cost hardware for bimanual teleoperation. *arXiv preprint arXiv:2405.02292*, 2024.
- [4] C. Chi, Z. Xu, S. Feng, E. Cousineau, Y. Du, B. Burchfiel, R. Tedrake, and S. Song. Diffusion policy: Visuomotor policy learning via action diffusion. In *Robotics: Science and Systems (RSS)*, 2023.
- [5] J. Engel, K. Somasundaram, M. Goesele, A. Sun, A. Gamino, A. Turner, A. Talattof, A. Yuan, B. Souti, B. Meredith, C. Peng, C. Sweeney, C. Wilson, D. Barnes, D. DeTone, D. Caruso, D. Valleroy, D. Ginpalli, D. Frost, E. Miller, E. Mueggler, E. Oleinik, F. Zhang, G. Somasundaram, G. Solaira, H. Lanaras, H. Howard-Jenkins, H. Tang, H. J. Kim, J. Rivera, J. Luo, J. Dong, J. Straub, K. Bailey, K. Eickenhoff, L. Ma, L. Pesqueira, M. Schwesinger, M. Monge, N. Yang, N. Charron, N. Raina, O. Parkhi, P. Borschowa, P. Moulon, P. Gupta, R. Mur-Artal, R. Pennington, S. Kulkarni, S. Miglani, S. Gondi, S. Solanki, S. Diener, S. Cheng, S. Green, S. Saarinen, S. Patra, T. Mourikis, T. Whelan, T. Singh, V. Balntas, V. Baiyya, W. Dreewes, X. Pan, Y. Lou, Y. Zhao, Y. Mansour, Y. Zou, Z. Lv, Z. Wang, M. Yan, C. Ren, R. De Nardi, and R. Newcombe. Project Aria: A new tool for egocentric multi-modal AI research. *arXiv preprint arXiv:2308.13561*, 2023.
- [6] S. Kareer, D. Patel, R. Punamiya, P. Mathur, S. Cheng, C. Wang, J. Hoffman, and D. Xu. EgoMimic: Scaling imitation learning via egocentric video. In *IEEE International Conference on Robotics and Automation (ICRA)*, 2025.
- [7] R. Punamiya, D. Patel, P. Aphiwetsa, P. Kuppili, L. Y. Zhu, S. Kareer, J. Hoffman, and D. Xu. EgoBridge: Domain adaptation for generalizable imitation from egocentric human data. In *Advances in Neural Information Processing Systems (NeurIPS)*, 2025.
- [8] R. Yang, Q. Yu, Y. Wu, R. Yan, B. Li, A.-C. Cheng, X. Zou, Y. Fang, X. Cheng, R.-Z. Qiu, H. Yin, S. Liu, S. Han, Y. Lu, and X. Wang. EgoVLA: Learning vision-language-action models from egocentric human videos. *arXiv preprint arXiv:2507.12440*, 2025.
- [9] R. Zheng, D. Niu, Y. Xie, J. Wang, M. Xu, Y. Jiang, F. Castañeda, F. Hu, Y. L. Tan, L. Fu, T. Darrell, F. Huang, Y. Zhu, D. Xu, and L. Fan. EgoScale: Scaling dexterous manipulation with diverse egocentric human data. *arXiv preprint arXiv:2602.16710*, 2026.
- [10] M. Lepert, J. Fang, and J. Bohg. Phantom: Training robots without robots using only human videos. In *Conference on Robot Learning (CoRL)*, 2025.

- [11] V. Liu, A. Adeniji, H. Zhan, S. Haldar, R. Bhirangi, P. Abbeel, and L. Pinto. EgoZero: Robot learning from smart glasses. *arXiv preprint arXiv:2505.20290*, 2025.
- [12] H. Bharadhwaj, R. Mottaghi, A. Gupta, and S. Tulsiani. Track2Act: Predicting point tracks from internet videos enables generalizable robot manipulation. In *European Conference on Computer Vision (ECCV)*, 2024.
- [13] S. Haldar and L. Pinto. Point policy: Unifying observations and actions with key points for robot manipulation. In *Conference on Robot Learning (CoRL)*, 2025.
- [14] C. Wang, L. Fan, J. Sun, R. Zhang, L. Fei-Fei, D. Xu, Y. Zhu, and A. Anandkumar. MimicPlay: Long-horizon imitation learning by watching human play. In *Conference on Robot Learning (CoRL)*, 2023.
- [15] G. Li, Y. Lyu, Z. Liu, C. Hou, J. Zhang, and S. Zhang. H2R: A human-to-robot data augmentation for robot pre-training from videos. *arXiv preprint arXiv:2505.11920*, 2025.
- [16] M. Xu, Z. Xu, Y. Xu, C. Chi, G. Wetzstein, M. Veloso, and S. Song. Flow as the cross-domain manipulation interface. In *Conference on Robot Learning (CoRL)*, 2024.
- [17] V. Jain, M. Attarian, N. J. Joshi, A. Wahid, D. Driess, Q. Vuong, P. R. Sanketi, P. Sermanet, S. Welker, C. Chan, I. Gilitschenski, Y. Bisk, and D. Dwibedi. Vid2Robot: End-to-end video-conditioned policy learning with cross-attention transformers. In *Robotics: Science and Systems (RSS)*, 2024.
- [18] T. Z. Zhao, V. Kumar, S. Levine, and C. Finn. Learning fine-grained bimanual manipulation with low-cost hardware. In *Robotics: Science and Systems (RSS)*, 2023.
- [19] Y. Lipman, R. T. Q. Chen, H. Ben-Hamu, M. Nickel, and M. Le. Flow matching for generative modeling. In *International Conference on Learning Representations (ICLR)*, 2023.
- [20] Y. Liu, A. Gupta, P. Abbeel, and S. Levine. Imitation from observation: Learning to imitate behaviors from raw video via context translation. In *IEEE International Conference on Robotics and Automation (ICRA)*, 2018.
- [21] L. Smith, N. Dhawan, M. Zhang, P. Abbeel, and S. Levine. AVID: Learning multi-stage tasks via pixel-level translation of human videos. In *Robotics: Science and Systems (RSS)*, 2020.
- [22] M. Lepert, J. Fang, and J. Bohg. Masquerade: Learning from in-the-wild human videos using data-editing. *arXiv preprint arXiv:2508.09976*, 2025.
- [23] J. Shi, Z. Zhao, T. Wang, I. Pedroza, A. Luo, J. Wang, J. Ma, and D. Jayaraman. ZeroMimic: Distilling robotic manipulation skills from web videos. In *IEEE International Conference on Robotics and Automation (ICRA)*, 2025.
- [24] C.-C. Hsu, B. Wen, J. Xu, Y. Narang, X. Wang, Y. Zhu, J. Biswas, and S. Birchfield. SPOT: SE(3) pose trajectory diffusion for object-centric manipulation. *arXiv preprint arXiv:2411.00965*, 2024.
- [25] R. Suvorov, E. Logacheva, A. Mashikhin, A. Remizova, A. Ashukha, A. Silvestrov, N. Kong, H. Goka, K. Park, and V. Lempitsky. Resolution-robust large mask inpainting with Fourier convolutions. In *IEEE/CVF Winter Conference on Applications of Computer Vision (WACV)*, 2022.
- [26] S. Liu, Z. Zeng, T. Ren, F. Li, H. Zhang, J. Yang, Q. Jiang, C. Li, J. Yang, H. Su, J. Zhu, and L. Zhang. Grounding DINO: Marrying DINO with grounded pre-training for open-set object detection. In *European Conference on Computer Vision (ECCV)*, 2024.

- [27] N. Ravi, V. Gabeur, Y.-T. Hu, R. Hu, C. Ryali, T. Ma, H. Khedr, R. Rädle, C. Rolland, L. Gustafson, E. Mintun, J. Pan, K. V. Alwala, N. Carion, C.-Y. Wu, R. Girshick, P. Dollár, and C. Feichtenhofer. SAM 2: Segment anything in images and videos. *arXiv preprint arXiv:2408.00714*, 2024.
- [28] N. Karaev, I. Rocco, B. Graham, N. Neverova, A. Vedaldi, and C. Rupprecht. CoTracker: It is better to track together. In *European Conference on Computer Vision (ECCV)*, 2024.
- [29] Z. Wang, Z. Zhang, J. Xu, J. Wang, T. Pang, C. Du, H. Zhao, and Z. Zhao. Orient anything V2: Unifying orientation and rotation understanding. In *Advances in Neural Information Processing Systems (NeurIPS)*, 2025.
- [30] Y. Zhou, C. Barnes, J. Lu, J. Yang, and H. Li. On the continuity of rotation representations in neural networks. In *IEEE/CVF Conference on Computer Vision and Pattern Recognition (CVPR)*, 2019.
- [31] X. Liu, C. Gong, and Q. Liu. Flow straight and fast: Learning to generate and transfer data with rectified flow. In *International Conference on Learning Representations (ICLR)*, 2023.
- [32] G. Pavlakos, D. Shan, I. Radosavovic, A. Kanazawa, D. Fouhey, and J. Malik. Reconstructing hands in 3D with transformers. In *IEEE Conference on Computer Vision and Pattern Recognition (CVPR)*, 2024.
- [33] C. Lugaresi, J. Tang, H. Nash, C. McClanahan, E. Uboweja, M. Hays, F. Zhang, C.-L. Chang, M. G. Yong, J. Lee, W.-T. Chang, W. Hua, M. Georg, and M. Grundmann. MediaPipe: A framework for building perception pipelines. *arXiv preprint arXiv:1906.08172*, 2019.

Appendix

A Data Collection Details

A.1 Aria Gen1 Glasses

Aria Gen1 recording configuration. We record every human demonstration with Project Aria Gen1 glasses, configured through the official Project Aria Mobile App with the sensor profile listed below:

- **RGB:** 30 fps at 2 MP.
- **SLAM:** 2× monochrome cameras, 30 fps at VGA.
- **ET (eye tracking):** 2× cameras, 10 fps at QVGA.
- **IMUs:** two 6-axis IMUs sampled at 1000 Hz and 800 Hz.
- **Magnetometer, barometer, 7-mic audio array, GPS, Wi-Fi, and BLE:** all enabled for synchronization metadata and environmental context.

All streams are hardware-timestamped on-device and synchronized to a common Aria clock, so every modality is time-aligned at the millisecond level.

Aria Machine Perception Services. On top of the raw recordings, Aria’s cloud-hosted *Machine Perception Services* (MPS) [5] post-process each capture into metric, ready-to-use signals. Two MPS outputs are critical for our pipeline:

- *Closed-loop trajectory.* The closed-loop SLAM output fuses the two monochrome SLAM cameras and the two IMUs and applies loop closure plus global optimization to yield a globally consistent, drift-corrected 6-DoF device trajectory in a gravity-aligned world frame. We query this trajectory at every RGB frame to obtain the calibrated camera extrinsics used for triangulation (App. B.1) and to lift every hand keypoint into the world frame consumed by ICT (Sec. 3.3).
- *Hand tracking.* The MPS hand tracker jointly processes the stereo SLAM cameras to produce 21 3D keypoints per hand (five per finger plus the wrist), reported directly in the world frame with per-keypoint confidence scores. This supplies the 3D hand skeleton consumed by our hand-to-gripper retargeting (App. B.3).

Together, the closed-loop trajectory and the hand tracker provide a metric 6-DoF camera pose and a 3D hand skeleton at every frame, without any calibration or scene instrumentation beyond wearing the glasses.

A.2 Task Details

We evaluate HumanEgo on four real-world manipulation tasks spanning pick-and-place, multi-step bimanual coordination, contact-rich reasoning, and sustained rotational control (Fig. 3). For each task we describe the scene, per-trial randomization, target behavior, and success/failure criteria used to score the 40 trials per condition reported in the main paper.

Serve Bread. *Scene.* A croissant and a dinner plate sit on a tabletop, plate on the left and bread on the right. *Randomization.* Across trials we independently randomize (i) the horizontal offset between the two objects, sampled from $[0, 50]$ cm, and (ii) their depths along the table’s front-back axis, so the pair is generally *not* colinear. The right arm starts from an arbitrary, non-aligned pose above the bread. *Target behavior.* Grasp the croissant from above, lift it clear of the table, transport it to a release pose above the center of the plate, and open the gripper. *Success.* The croissant comes to rest on the plate, in any orientation. *Failure.* (a) the bread ends up outside the plate (on the table, draped over the rim, or knocked off); or (b) the bread slips from the gripper during transport.

Downstack Cups. *Scene.* Three cups of distinct colors on a tabletop: a *white* cup at bottom-right, a *dark-blue* cup at bottom-left, and a *light-blue* cup stacked on top of the white cup. The table



Fig. 11: Data collection setup.

height and the absolute position of the cup group are varied across trials. *Randomization.* The horizontal gap between the white and dark-blue cups is drawn from $[0, 1]$ cm; the light-blue cup is jittered left/right within $[0, 2]$ cm on top of the white cup. *Target behavior.* A three-step sequence: (1) *Topple*—knock the light-blue cup sideways so it lands on top of the dark-blue cup; (2) *Grasp*—swing over to the white cup and grasp it from above; (3) *Cover*—lower the white cup onto the dark-blue/light-blue stack and release, forming a three-cup tower on the left (dark-blue / light-blue / white, bottom-to-top). *Success.* The three cups end in the intended stable stack on the left. *Failure.* (a) the light-blue cup is never contacted; (b) it is toppled but does not land on the dark-blue cup; (c) the white cup is not grasped; or (d) the white cup is not correctly placed on the stack (misses it, topples it, or lands off-axis so the tower collapses). Early errors compound, so the policy must succeed at every sub-stage.

Water Flowers. *Scene.* A wall-mounted faucet stands at the front of the workspace, with a sunken sink recessed ~ 10 cm below the tabletop directly underneath. A flower pot filled with fresh flowers sits inside the sink. *Randomization.* The pot is placed at one of three qualitatively different positions in the sink (top-left, middle, or bottom-right); the faucet is free to rotate about its vertical axis within $[-15^\circ, +15^\circ]$. *Target behavior.* Coordinated bimanual execution with strict temporal ordering. **Left arm (spray head):** grasp the pull-out spray head, pull it ~ 15 cm downward out of the faucet socket, and hold the nozzle 3–5 cm above the center of the flower pot, pointed downward. **Right arm (handle):** remain visible in a stationary pre-grasp pose near the faucet handle while the left arm works; once the left arm is in place, grasp the handle and flick it to the right by 3–5 cm to open the valve, so water flows onto the flowers. *Success.* The left arm holds the spray head over the pot while the right arm has opened the valve and water pours onto the flowers. *Failure.* *Left arm:* (a) the spray head is not grasped or not pulled down; (b) it slips during pull-out or transport; or (c) it is not positioned directly above the pot. *Right arm:* (a) the handle is not grasped; or (b) it is not flicked far enough to open the valve, or slips before water flows.

Adjust Table. *Scene.* The operator faces an adjustable table whose height is controlled by a hand crank protruding from its side, oriented roughly horizontally. *Randomization.* The initial angle of the crank handle about its rotation axis is jittered by $\pm 10^\circ$ around horizontal. *Target behavior.* The right arm (1) approaches the crank handle from an arbitrary initial pose and grasps it firmly, then (2) performs a continuous *counter-clockwise* rotation about the crank axis, completing three full revolutions ($3 \times 360^\circ$) without releasing the handle. *Success.* All three revolutions are completed while the grasp is maintained throughout. *Failure.* (a) the handle is never grasped; or (b) the handle slips from the gripper during the rotation, before three full revolutions are completed.

B Preprocessing Details

B.1 Triangulation

Aria Gen1 glasses lack a depth sensor, so we recover each object’s 3D position by triangulating tracked 2D keypoints across frames, treating the moving head-mounted camera as a multi-view system with calibrated extrinsics given by the 6-DoF Aria MPS SLAM pose [5]. This requires the object to remain stationary during the observation window; once manipulation begins, the object is free to move.

Pre-episode scene sweep. Multi-view triangulation requires the same 3D point to be seen from sufficiently different viewpoints, yet during manipulation the head-mounted camera is often nearly stationary while only the hands move, collapsing the effective camera baseline. We therefore prefix every demonstration with a short *scene sweep*: the demonstrator keeps the scene static and slowly moves their head for ~ 1 – 2 seconds (~ 30 – 60 frames), using either a horizontal left-to-right pan or a forward walk-in toward the object, before proceeding to the actual manipulation.

Multi-view triangulation from 2D tracks. For each object we detect it in the first sweep frame with Grounding DINO [26], segment it with SAM2 [27], sample N keypoints on the resulting mask, and track them through the F sweep frames with CoTracker3 [28]. Let $K \in \mathbb{R}^{3 \times 3}$ be the RGB intrinsics, $T_i = [R_i | t_i]$ the camera-to-world SLAM pose of frame i , and $P_i = K [R_i^\top | -R_i^\top t_i] \in$

$\mathbb{R}^{3 \times 4}$ the corresponding world-to-image projection. A track $\{\mathbf{u}_n^{(i)}\}_{i=1}^F$ and the unknown 3D point $\mathbf{X}_n \in \mathbb{R}^4$ (homogeneous) satisfy $\mathbf{u}_n^{(i)} \times P_i \mathbf{X}_n = 0$, which yields two linear equations per frame:

$$\begin{bmatrix} u_n^{(i)} \mathbf{p}_3^{(i)\top} - \mathbf{p}_1^{(i)\top} \\ v_n^{(i)} \mathbf{p}_3^{(i)\top} - \mathbf{p}_2^{(i)\top} \end{bmatrix} \mathbf{X}_n = \mathbf{0}, \quad (4)$$

where $\mathbf{p}_j^{(i)\top}$ is the j -th row of P_i . Stacking (4) across all F frames gives a $2F \times 4$ system $A_n \mathbf{X}_n = \mathbf{0}$; we solve it in the least-squares sense via SVD by taking the right singular vector of A_n with the smallest singular value and dehomogenizing to recover $\mathbf{x}_n \in \mathbb{R}^3$. The object position is then the centroid $\mathbf{p}_{\text{obj}} = \frac{1}{N} \sum_{n=1}^N \mathbf{x}_n$, which cancels per-point triangulation noise.

B.2 Phase Detection

A raw Aria recording interleaves active manipulation with non-manipulation segments—walking up to the workspace, the pre-episode scene sweep (App. B.1), and stepping back once the task ends. Only the manipulation portions carry clean hand–object dynamics, so we run an automatic *phase detection* step that segments every recording into kinematic modes and keeps only the manipulation frames for training.

Phase taxonomy. Each frame is assigned one of five modes: (0) MANIP—demonstrator stands still and actively manipulates the scene; (1) FORWARD—linear walking; (2) ROTATE—in-place head/body rotation (*e.g.* the scene sweep); (3) TRANSITION—short buffers between adjacent modes; (4) FINISHED—sustained final hold at the end of the recording.

Segmentation signals and training-data selection. Phases are computed from two streams: the 6-DoF head trajectory from Aria SLAM (body motion) and the 3D hand trajectory from the hand tracker (manipulation motion). A frame enters MANIP when the head linear and angular speeds simultaneously fall below $v_{\text{stop}}=0.03$ m/s and $w_{\text{stop}}=0.15$ rad/s for ≥ 15 consecutive frames; ROTATE requires $\|\boldsymbol{\omega}_{\text{head}}\| > 0.10$ rad/s with $\|\mathbf{v}_{\text{head}}\| < 0.08$ m/s; FORWARD collects the remaining high-linear-speed frames; TRANSITION fills a 10-frame buffer at every mode change; and FINISHED is declared once the trailing stop lasts for ≥ 30 frames. We additionally refine MANIP with hand kinematics: a candidate frame is demoted to TRANSITION if the average hand speed exceeds 0.15 m/s over a 5-frame window, trimming reaching/retracting motion away from the manipulation core. The training pipeline then keeps only MANIP (0) and FINISHED (4), dropping FORWARD, ROTATE, and TRANSITION, so the scene sweep, navigation, and mode-change buffers never reach the training signal.

B.3 Hand-to-Gripper Transfer

To treat a human egocentric video as robot data, every frame of the demonstration must carry an end-effector target that a parallel-jaw robot can actually execute. The human hand, however, has 21 articulated keypoints and a morphology very different from a 2-finger gripper, so the raw hand pose cannot be passed through directly. We therefore *retarget* the hand into a virtual gripper—a 6-DoF SE(3) pose plus a 1-DoF grasp scalar—derived from a few anatomically stable keypoints after a short motion-optimization pipeline.

Hand keypoint extraction. We start from the 21-keypoint hand skeleton produced by Aria MPS [5], which fuses the stereo SLAM cameras and the on-device IMU to recover every keypoint’s 3D position in the SLAM world frame at each frame. For retargeting we use only five keypoints per hand (Fig. 12): the *wrist*, *thumb MCP*, *thumb tip*, *index MCP*, and *index tip*.

Motion optimization. Raw MPS keypoints are noisy and occasionally drop frames, and feeding them directly into the SE(3) construction produces jittery, flip-prone trajectories. We therefore run

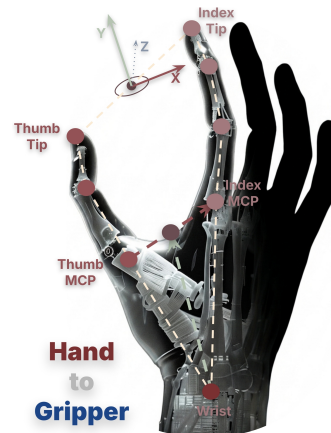


Fig. 12: Hand-to-gripper mapping.

a short optimization pipeline: (1) *Confidence masking*—we drop any keypoint whose MPS confidence falls below 0.8 and discard detection segments shorter than 30 consecutive frames as likely ghost detections; (2) *Gap interpolation*—short missing intervals (≤ 10 frames) are filled with linear interpolation on positions and SLERP on orientations, so the later smoother sees a dense sequence; (3) *Savitzky–Golay position smoothing*—we apply an SG filter with window size 21 and polynomial order 2 to the five retarget keypoints, removing high-frequency jitter while preserving manipulation-relevant accelerations; (4) *EMA orientation smoothing*—we apply an exponential moving average with $\alpha_x = \alpha_y = 0.15$ to the X - and Y -axes of the gripper frame (defined below), re-orthonormalize via Gram–Schmidt after each update, and enforce sign consistency across adjacent frames to prevent spurious 180° flips.

End-effector position. We take the midpoint of the thumb tip and the index tip as the gripper position, which naturally corresponds to the center of a parallel-jaw grasp:

$$\mathbf{p}_{ee} = \frac{1}{2}(\mathbf{p}_{\text{thumb tip}} + \mathbf{p}_{\text{index tip}}). \quad (5)$$

End-effector orientation. Choosing an orientation that is both *accurate* and *stable through pinch grasps* is the subtle part of retargeting; two natural alternatives both fail. (i) *Raw wrist pose*: using the MPS wrist orientation directly as the gripper frame is inaccurate, because the anatomical wrist frame is not aligned with the thumb–index action axis that the gripper actually uses. (ii) *Wrist-to-fingertip-midpoint*: defining the forward axis as $\text{wrist} \rightarrow \text{mid}(\text{thumb tip}, \text{index tip})$ and the jaw axis as $\text{thumb tip} \rightarrow \text{index tip}$ works when the hand is open but becomes *degenerate at the moment of grasp*—the two fingertips converge to nearly the same point, so the jaw axis collapses to a near-zero vector and the frame is ill-defined. We instead build the gripper frame from the MCP joints, which remain well-separated throughout the full pinch cycle. Writing \mathbf{p}_w , \mathbf{p}_{MCP} , \mathbf{p}_{iMCP} for the wrist, thumb-MCP, and index-MCP positions, we construct

$$\mathbf{x}_{ee} = \widehat{\mathbf{p}_{\text{iMCP}} - \mathbf{p}_{\text{MCP}}}, \quad \mathbf{y}_{ee} = \tilde{\mathbf{y}} - (\tilde{\mathbf{y}}^\top \mathbf{x}_{ee}) \mathbf{x}_{ee}, \quad \mathbf{z}_{ee} = \mathbf{x}_{ee} \times \mathbf{y}_{ee}, \quad (6)$$

where $\tilde{\mathbf{y}} = \frac{1}{2}(\mathbf{p}_{\text{MCP}} + \mathbf{p}_{\text{iMCP}}) - \mathbf{p}_w$ is the raw wrist-to-MCP-midpoint vector and $\widehat{\cdot}$ denotes unit normalization. Intuitively, \mathbf{y}_{ee} is the forward axis (wrist \rightarrow MCP midpoint), \mathbf{x}_{ee} is the jaw opening axis (thumb MCP \rightarrow index MCP), and \mathbf{z}_{ee} is the orthogonal complement. The rotation $R_{ee} = [\mathbf{x}_{ee} \mid \mathbf{y}_{ee} \mid \mathbf{z}_{ee}] \in \text{SO}(3)$ together with the position \mathbf{p}_{ee} from Eq. (5) gives the $\text{SE}(3)$ end-effector pose T_{ee} . Because the two MCPs never collapse to each other during a pinch, this construction stays numerically stable across the full grasp/release cycle.

Gripper aperture. We derive the 1-DoF gripper command from the thumb–index fingertip distance:

$$g = \text{clip}\left(\frac{\|\mathbf{p}_{\text{thumb tip}} - \mathbf{p}_{\text{index tip}}\| - d_{\min}}{d_{\max} - d_{\min}}, 0, 1\right), \quad (7)$$

where d_{\min} and d_{\max} are the closed and fully-open fingertip distances calibrated per user. The normalized g is then median-filtered and run through a short flicker-suppression pass to produce a clean open/close command stream, and binarized at deployment.

C Training Details

C.1 Flow Matching Policy

Velocity field and loss. We train a conditional flow matching [19] policy that maps a Gaussian prior $\mathbf{x}_0 \sim \mathcal{N}(0, I)$ to the ground-truth bimanual action chunk $\mathbf{x}_1 \in \mathbb{R}^{K \times D_a}$ along the linear path $\mathbf{x}_t = (1-t)\mathbf{x}_0 + t\mathbf{x}_1$ with flow time $t \sim \mathcal{U}(0, 1)$. The target velocity is the constant displacement $\mathbf{v}_{\text{target}} = \mathbf{x}_1 - \mathbf{x}_0$, and the flow-matching loss is an MSE over the predicted velocity with dimension-wise reweighting: $w_p=5$ on position, $w_r=1$ on 6D rotation, and $w_g=10$ on the grasp logit. We also support an optimal-transport matching variant (OT-CFM) that solves a Hungarian assignment between noise and action samples within each mini-batch before computing the loss, producing straighter target flows; we leave it off by default since we did not find consistent wins on our tasks.

Network. The velocity field v_θ is a 6-layer, 8-head transformer decoder with embedding dimension 384 and dropout 0.05. Each action-chunk token attends (via self-attention) to the rest of the chunk and (via cross-attention) to the conditioning context. Context is built from two streams: (i) the RGB frame, embedded with a 16×16 patch embedding on a 240×320 input and a sinusoidal time embedding fused through a small MLP; and (ii) the state tokens, i.e., the per-entity ICT tokens described in Sec. 3.3, linearly projected to 384 channels.

Auxiliary heads. Three dense auxiliary objectives share the context encoder with the velocity field (Sec. 3.4). The *object-dynamics* head predicts the 9-D future pose trace of the manipulated object and is trained with $0.5(w_p, w_r)$ -weighted MSE; the *2D visual-foresight* head emits $K \times 3 \times 2$ normalized image coordinates of three anchor keypoints through a shallow deconvolution stack with loss weight $w_f=20$; and the *temporal-consistency* head predicts the hand tokens K steps ahead with a masked MSE weighted by $w_c \in [0.1, 1.0]$. All three targets are produced automatically by the perception pipeline, so each demonstration yields a dense multi-task signal without extra labeling.

Additional tricks. Two lightweight training tricks further stabilize learning from minutes of data. *Region attention* biases the image cross-attention toward the currently active manipulation anchor: given the anchor’s 2D image projection (u_0, v_0) , we multiply the attention logits by a Gaussian spotlight

$$w(u, v) = \exp\left(-\frac{(u - u_0)^2 + (v - v_0)^2}{2\sigma^2}\right), \quad (8)$$

whose spatial scale σ is a learnable parameter, softly focusing the encoder on task-relevant image regions without hard-cropping. *State-noise injection* perturbs every hand token during training, $\tilde{s}_t = s_t + \epsilon$ with $\epsilon \sim \mathcal{N}(\mathbf{0}, \Sigma_s)$ and separate standard deviations on the position, 6D rotation, and grasp channels, which makes the policy robust to the small perception noise it encounters at deployment.

Optimization recipe. We train with AdamW at a base learning rate of 10^{-4} , cosine decay with 200-step warmup, minimum-LR ratio 0.05, batch size 32, and 400 epochs. We clip gradient norm at 1.0, use bfloat16 mixed precision, and keep an exponential moving average of the weights with decay 0.999 for evaluation and deployment.

Data augmentation. To expand the effective training distribution from only ~ 40 min of human video per task, we apply a cocktail of augmentations on the fly in the dataloader, grouped into three families. (i) *Image augmentations* on the RGB stream. Photometric jitter ($p=0.8$) randomly perturbs brightness (± 0.20), contrast (± 0.20), and gamma (± 0.15), adds Gaussian pixel noise ($\sigma=0.02$), optionally converts the frame to grayscale ($p=0.1$), and jitters HSV hue by ± 10 and saturation by $[0.6, 1.4]$. A random resized crop ($p=0.5$) draws a sub-window with scale in $[0.7, 1.0]$ and aspect ratio in $[0.9, 1.1]$ before resizing back to the network input size. A Gaussian blur with a 3×3 kernel is applied with $p=0.15$, and random erasing ($p=0.5$) overlays 3–8 black cutout patches each covering 5–20% of the frame area. (ii) *Action-target augmentation.* We additively perturb every target pose in the action chunk with Gaussian noise— $\sigma_{\text{pos}}=1$ mm on translation and $\sigma_{\text{rot}}=0.5^\circ$ on rotation—before the flow-matching loss is computed, which regularizes the velocity field against small tracking noise in the labels. (iii) *Temporal augmentation.* With $p=0.5$ we apply *sub-step interpolation*: adjacent state/action frames are linearly blended at a random $\alpha \in [0, 1]$, effectively densifying the temporal grid at no extra collection cost.

D Inference Details

D.1 Robot Inference Setup

Apart from the zero-shot generalization study (Sec. 4.3), all real-world experiments in the main paper use the single inference setup shown in Fig. 13: two Trosser WidowX AI arms mounted side-by-side on a shared workbench, forming a bimanual platform that handles both single-arm



Fig. 13: Robot inference setup.

and two-arm tasks without any hardware change between tasks. Each WidowX AI arm is a 6-DoF parallel-jaw manipulator with a ~ 1.5 kg payload at full reach and ± 1 mm end-effector repeatability. For visual input we use a single Intel RealSense D405 mounted top-down above the workspace; its RGB stream is the sole observation consumed by HumanEgo. Each WidowX AI arm also ships with a built-in wrist camera, but we deliberately do not use it for HumanEgo: the robot-teleoperation ACT baseline [18] in Sec. 4.1, in contrast, does consume the wrist cameras as part of its standard observation interface.

D.2 Flow Matching Rollout and Control

ODE rollout. At test time we integrate the learned velocity field with a fixed-step Euler solver using 20 inference steps: starting from a noise sample $\mathbf{x}_0 \sim \mathcal{N}(0, I)$ drawn once at policy load time, we iterate $\mathbf{x}_{t+\Delta t} \leftarrow \mathbf{x}_t + v_\theta(\mathbf{x}_t, t, s_t) \Delta t$ with $\Delta t = 1/20$, yielding a $K=50$ -step bimanual action chunk in one forward pass per re-plan. Predictions are unpacked dimension-wise into per-hand position, 6D rotation, and grasp logit, with positions denormalized by the dataset mean/std, rotations projected back to $SO(3)$ via *normalize-then-Gram-Schmidt* on the 6D representation, and grasps passed through a sigmoid.

Action chunking and control. The controller re-plans at every cycle (10 Hz), keeping at most one prediction in history and executing one action per cycle. A step stride of 2 sub-samples the chunk so the effective executed rate is 5 Hz, and a look-ahead offset of 25 steps lets the controller query the chunk slightly ahead of the current execution index to mask planning latency. For grasp we use an any-over-horizon rule: the gripper closes as soon as *any* step in the current chunk predicts a grasp probability above 0.6; an optional grasp-latch mode additionally locks the gripper closed after the first grasp event to prevent accidental mid-task releases.

Smoothing and safety. To hide small noise in the predicted $SE(3)$ stream we apply an EMA on positions ($\alpha=0.5$) and quaternion SLERP on rotations before streaming targets to the arms, and a trajectory-overlap blend (smoothing parameter 12) to avoid jerky starts/stops between consecutive chunks. Finally, a safety cage limits each per-cycle target displacement to ≤ 0.08 m in position and ≤ 0.02 rad in rotation to guard against sudden outliers; we did not observe any safety-cage clamp during normal rollouts in our experiments.

E Additional Experiments Analysis

E.1 Hand Tracking Method Study

Setup. ICT consumes 3D hand keypoints as input, so the quality of the upstream hand tracker directly affects what the policy can learn. We isolate this dependency on Serve Bread by holding everything else constant—the same 45 demonstrations (30 min total), the same HumanEgo architecture, the same training recipe—and varying only the hand-tracking module that produces the action labels. We compare four trackers spanning the dominant design choices in the literature: (1)

Aria-MPS [5], our default, which fuses the two wide-FoV *monochrome SLAM* cameras with the on-device IMU through Meta’s MPS pipeline to recover metric 3D keypoints—note that the central RGB camera is used only for video logging, not for hand tracking; (2) **WiLoR**, a transformer that regresses MANO parameters from a single RGB crop per frame; (3) **HaMeR** [32], a strong monocular RGB estimator that also predicts MANO parameters but processes frames independently; and (4) **MediaPipe** [33], a lightweight monocular RGB pipeline whose 3D outputs are root-relative and have to be lifted with the camera depth. For each tracker we re-run the data preprocessing, train HumanEgo from scratch, and evaluate 40 real-world trials on Serve Bread (Fig. 15). Aria-MPS is treated as the reference for all alignment-style metrics in Fig. 14.

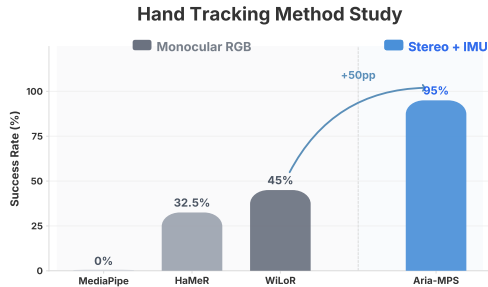


Fig. 15: Hand Tracking Method Study.

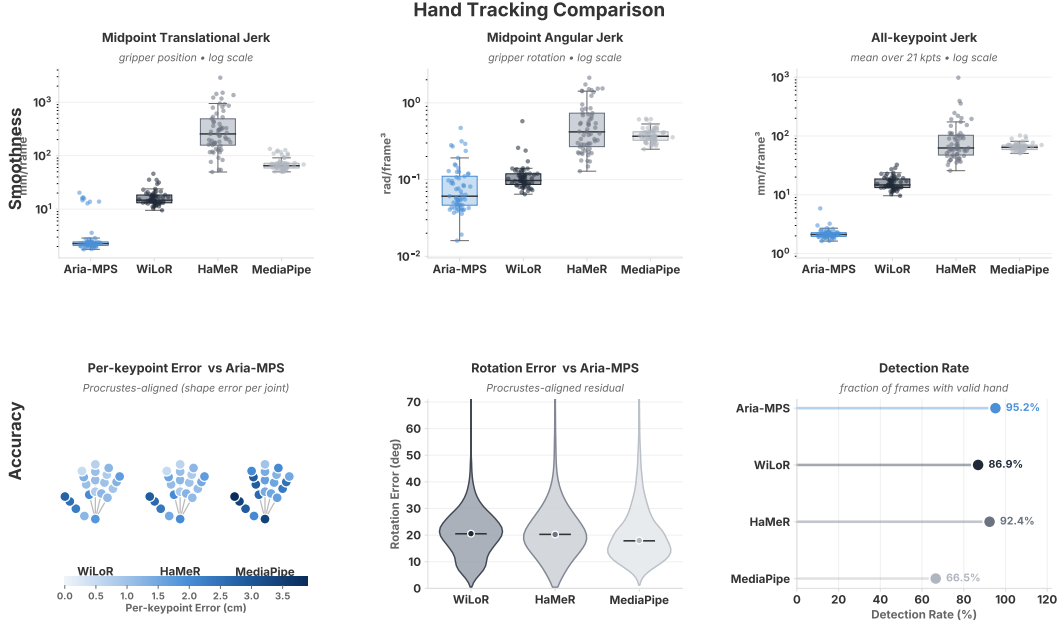


Fig. 14: **Hand tracking comparison on Serve Bread** (45 demonstrations, ~ 45 k frames). *Top*—*Smoothness*: per-frame jerk of the gripper midpoint (translational and angular) and of all 21 keypoints (lower is better, log scale). *Bottom*—*Accuracy vs. Aria-MPS*: per-keypoint shape error after Procrustes alignment, residual rotation error after subtracting the systematic frame offset, and fraction of frames with a valid hand detection.

Results. Fig. 15 shows real-world success collapsing by $95 \rightarrow 45 \rightarrow 32.5 \rightarrow 0\%$ as we move from stereo Aria-MPS to monocular trackers, and Fig. 14 explains why. We highlight four observations.

Stereo depth is decisive for downstream success. Real-world success drops from 95 % (Aria-MPS) to at most 45 % (WiLoR) the moment we replace stereo with monocular RGB. Monocular networks are inherently scale-ambiguous along the depth axis, producing a 5–11 cm systematic depth offset that propagates directly into the ICT reference frame, so the policy never learns a consistent grasp.

Smoothness and tracking persistence—not pose accuracy per se—separate the surviving baselines. After Procrustes alignment the per-keypoint residual error is nearly identical for HaMeR and WiLoR (1.4 cm vs. 1.4 cm; both dominated by the shared MANO inductive bias) and only modestly worse for MediaPipe (2.2 cm). Yet WiLoR (45 %) clearly beats HaMeR (32.5 %). The gap is explained by the smoothness panels: WiLoR’s gripper-midpoint jerk is more than an order of magnitude lower than HaMeR’s—its per-frame predictions happen to be far more temporally stable—and its detection rate is 86.9 % vs. MediaPipe’s 66.5 %. A jittery or intermittently missing trajectory teaches the policy incoherent action labels.

The MANO prior is a double-edged sword. HaMeR and WiLoR show essentially identical per-keypoint Procrustes residuals (Fig. 14, bottom-left): the colored patterns on the two hand skeletons are visually indistinguishable. This is not a coincidence—both networks regress MANO pose parameters and inherit the same canonical bone proportions. The shared shape prior means their residual shape errors are correlated by construction, while methods without a parametric constraint (Aria-MPS, MediaPipe) deviate in different ways. This explains why pose accuracy alone is a poor predictor of downstream policy success.

MediaPipe fails entirely. With 0 % real-world success and only 66.5 % detection rate, MediaPipe cannot produce coherent action labels even with the ICT representation absorbing some noise. Its 3D output is root-relative and must be lifted with the camera depth, and the lift collapses the hand thickness to ~ 7 cm (vs. ~ 16 cm for Aria), flattening the pose information that ICT relies on.

Together these results point to a clear practical message: invest in the perception frontend. A more accurate hand tracker—especially one that exploits stereo or learned depth—is the highest-leverage upgrade for any policy that operates on hand-derived spatial tokens.

E.2 Human-Robot Co-Training Study

Setup. The data-efficiency study (Sec. 4.2) showed that human demonstrations are roughly $3.75\times$ more sample-efficient than robot teleoperation *at the same total collection time*. Here we ask the complementary question: when both modalities are available, what is the best mixing ratio? We hold the total collection time fixed at 30 min and vary the fraction of *human* data from 0% (pure robot teleoperation, ~ 45 teleop episodes) to 100% (pure human egocentric video, ~ 45 egocentric demos) in 25-pp steps. Each batch is sampled with the corresponding ratio, so the policy sees both modalities in the intended proportion at every gradient step. The architecture, optimizer, schedule, and number of training steps are kept identical across the five conditions; only the data mixture changes. We evaluate 40 real-world trials on Serve Bread *per condition*.

Results. Real-world success increases *monotonically* as the human-data ratio grows: 65 \rightarrow 72.5 \rightarrow 77.5 \rightarrow 90 \rightarrow 95% for human ratios of 0/25/50/75/100% (Fig. 16). The pure-human policy improves over the pure-robot policy by +30 pp—a gap larger than that between most of our baselines. We extract two main findings.

Even a small slice of human data dominates.

Replacing just 25% of the robot teleop with egocentric video already lifts success from 65% to 72.5% (+7.5 pp), even though the absolute amount of robot data drops from 30 min to 22.5 min in that condition. A naive “more data is always better” view would predict the opposite: less robot data should hurt. Instead the policy improves, indicating that the marginal robot minutes contribute less signal than the marginal human minutes. This reproduces the data-efficiency conclusion (Sec. 4.2) at the level of the gradient step: the policy is happier learning from a small amount of clean egocentric video than from a large amount of teleop trajectory.

The more human data, the better—no co-training sweet spot. Across all four transitions the curve only goes up, and the pure human policy is the global maximum. We find no “sweet spot” where mixing in robot data outperforms the human-only condition—in fact 75/25 (90%) is already 5 pp below 100/0 (95%), so adding even 7.5 min of robot teleoperation actively erodes a 22.5 min human dataset. We attribute this to the higher per-minute information density of human demonstrations documented in Sec. 4.2 (Fig. 6): human videos exhibit higher signal-to-noise ratio, an order-of-magnitude smoother trajectories, near-zero idle time, and broader spatial coverage than robot teleoperation. At a fixed compute and time budget, the policy is best served by spending every minute on human data. Combined with the embodiment-invariance of ICT, this means a practitioner deploying HumanEgo should not invest in robot teleoperation at all—the same budget collected as egocentric human video yields a strictly better policy.

E.3 Reference Frame Study

The choice of reference frame is a key design decision in ICT. We compare two strategies: (1) the *anchor frame*, in which every entity pose—as well as the action trajectory—is expressed relative to the first object grasped in the trajectory, and (2) the *camera frame* (used in our main experiments), in which all poses are expressed in the camera’s coordinate system. The two representations exhibit a clear trade-off whose balance shifts with the amount of training data (Fig. 17).

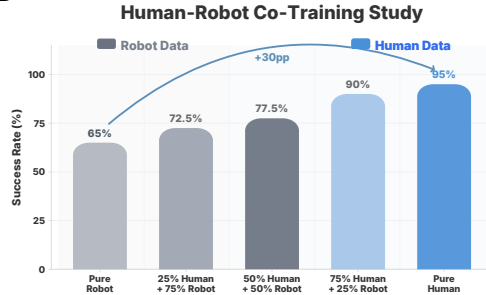


Fig. 16: Human-Robot Co-Training Study.

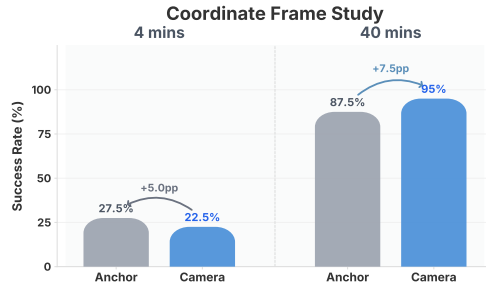


Fig. 17: Coordinate Frame Study.

Low-data regime: the anchor frame wins. With few training demonstrations, expressing the scene in the anchor frame substantially accelerates policy learning. Because the anchor frame ties spatial reasoning to a task-relevant object rather than to the camera, the model can recover the fundamental geometry of manipulation—in particular, the relative pose between the hand and the target object at the moment of contact—from far fewer demonstrations. This *grasping prior* is precisely the bottleneck that limits sample efficiency in many imitation learning settings, and the anchor frame supplies a strong inductive bias that bypasses it. The result is markedly better grasp success and downstream task completion when only a handful of trajectories are available.

Large-data regime: the camera frame catches up and surpasses anchor frame. As training data grows, the model has enough signal to recover the same relational geometry directly from camera-frame observations. At that point, the camera frame becomes the more reliable representation, for two reasons: (i) it is grounded in the raw sensor and is not contaminated by upstream perception errors, whereas (ii) the anchor frame inherits noise from the object detection and pose estimation modules (Grounding DINO, SAM2, Orient-Anything), whose errors directly perturb every transformed coordinate. Empirically, given sufficient data the camera-frame variant matches and modestly exceeds the anchor-frame variant on in-distribution evaluations, because the anchor-frame policy is ultimately bounded by the accuracy of its upstream object pose estimates.

The anchor frame’s enduring advantage: camera-pose invariance. Despite the asymptotic parity (or slight inferiority) in raw success rate, the anchor frame retains a property that the camera frame *cannot* offer: *deployment-time invariance to camera placement*. Because every coordinate is expressed relative to the object, the absolute position and orientation of the camera are irrelevant—the policy can be deployed with a camera mounted at any reasonable angle, height, or distance, and it will behave identically. In contrast, a camera-frame policy is tied to a specific viewpoint distribution and degrades sharply whenever the camera is repositioned, forcing every new mounting to trigger fresh data collection or fine-tuning.

F Hyperparameters

Table 1 consolidates every hyperparameter value that appears in the main paper and the appendix, grouped by pipeline stage. Unless explicitly noted, a single value is used across all four tasks, all training runs, and all real-world trials.

Table 1: **All hyperparameters used in HumanEgo.** Values are shared across the four tasks unless noted.

Parameter	Value
<i>Data Collection (App. A.1, App. A.2)</i>	
Demonstrations per task	60
Total human-video time per task	40 min
RGB stream rate / resolution	30 fps / 2 MP
SLAM cameras: count, rate, resolution	2, 30 fps, VGA
Eye-tracking cameras: count, rate, resolution	2, 10 fps, QVGA
IMU rates	1000 Hz, 800 Hz
Pre-episode scene-sweep duration	1–2 s
Scene-sweep frame count	30–60
<i>Phase Detection (App. B.2)</i>	
Head linear-speed stop threshold v_{stop}	0.03 m/s
Head angular-speed stop threshold w_{stop}	0.15 rad/s
Minimum stop-hold duration	15 frames
Rotate trigger w_{rot}	0.10 rad/s
Rotate max linear speed $v_{\text{rot,max}}$	0.08 m/s
Transition buffer	10 frames
Hand-velocity demotion threshold v_{hand}	0.15 m/s
Hand-velocity averaging window	5 frames
Finished-stop length	30 frames
<i>Hand-to-Gripper Retargeting (App. B.3)</i>	
Retarget keypoints per hand	5
MPS confidence threshold	0.8
Minimum detection segment	30 frames
Max gap for interpolation	10 frames
Savitzky–Golay window	21 frames
Savitzky–Golay polynomial order	2
EMA smoothing factor $\alpha_x = \alpha_y$	0.15
<i>Policy Network (App. C.1)</i>	
Transformer layers	6
Transformer attention heads	8
Transformer embedding dim	384
Dropout	0.05
RGB patch size	16×16
RGB input resolution	240×320
ICT token dim	29
Prediction horizon K	50
<i>Losses (App. C.1)</i>	
Position weight w_p	5
Rotation weight w_r	1
Grasp weight w_g	10
Object-dynamics weight (pos / rot)	$0.5 w_p / 0.5 w_r$
Visual-foresight weight w_f	20
Temporal-consistency weight w_c	[0.1, 1.0]
<i>Optimization (App. C.1)</i>	
Optimizer	AdamW
Base learning rate	1×10^{-4}
Warmup steps	200
Min-LR ratio	0.05
Batch size	32
Epochs	400

Continued on next page

Table 1 – continued from previous page

Parameter	Value
Gradient-norm clip	1.0
EMA decay	0.999
<i>Data Augmentation (App. C.1)</i>	
Photometric jitter probability	0.8
Brightness / contrast delta	$\pm 0.20 / \pm 0.20$
Gamma delta	± 0.15
Pixel noise σ	0.02
Grayscale probability	0.1
HSV hue jitter	± 10
HSV saturation range	[0.6, 1.4]
Random resized crop probability	0.5
Scale range	[0.7, 1.0]
Aspect-ratio range	[0.9, 1.1]
Gaussian blur probability	0.15
Kernel size	3×3
Random erasing probability	0.5
Number of holes	3–8
Per-hole area	5–20%
Target position noise σ_{pos}	1 mm
Target rotation noise σ_{rot}	0.5°
Sub-step interpolation probability	0.5
<i>Hardware (App. D.1)</i>	
Robot arms	2× Trossen WidowX AI
WidowX AI DoF	6
WidowX AI payload at full reach	~1.5 kg
WidowX AI end-effector repeatability	± 1 mm
Inference RGB camera	Intel RealSense D405 (top-mounted)
<i>Inference (App. D.2)</i>	
Euler ODE steps	20
Step size Δt	1/20
Executed action-chunk length	$K = 50$
Control-loop frequency	10 Hz
Action-step stride	2
Effective executed rate	5 Hz
Look-ahead offset	25 steps
Grasp probability threshold	0.6
Position smoothing EMA α	0.5
Rotation smoothing	quaternion SLERP
Trajectory-overlap smoothing parameter	12
Safety cage: max position step	0.08 m
Safety cage: max rotation step	0.02 rad
<i>Robot Teleoperation for ACT Baseline</i>	
Teleop control frequency (leader → follower)	200 Hz
Teleop recording frequency	30 Hz
Leader → follower EMA α	0.5
Top camera resolution	640×480
Wrist camera resolution	320×240
Action space	7-DoF joint positions
Proprioception dim	7
<i>ACT Baseline Training</i>	
Visual backbone	ResNet-18 (pretrained)
Embedding dim	256
Attention heads	8
Encoder / decoder layers	4 / 1
Feed-forward dim	2048
CVAE latent dim	32
Dropout	0.1
Prediction horizon K	50

Continued on next page

Table 1 – continued from previous page

Parameter	Value
Image input resolution	240×320
Batch size	24
Epochs	400
Base learning rate	1×10^{-4}
Weight decay	1×10^{-2}
Warmup steps	500
EMA decay	0.999
Action L1 weight w_{pos}	5.0
CVAE KL loss weight (annealed to)	10.0